ARTICLES
https://doi.org/10.1038/s41565-020-0729-y
nature nanotechnology

Probing photoelectrical transport in lead halide perovskites with van der Waals contacts

Yiliu Wang[1,6], Zhong Wan[1,6], Qi Qian[1,2,6], Yuan Liu[2,3], Zhuo Kang[4], Zheng Fan[3], Peiqi Wang[1], Yekan Wang[3], Chao Li[3], Chuancheng Jia[1], Zhaoyang Lin[1], Jian Guo[3], Imran Shakir[5], Mark Goorsky[3], Xidong Duan[2], Yue Zhang[4], Yu Huang[3] and Xiangfeng Duan[1]✉

Lead halide perovskites have attracted increasing interest for their exciting potential in diverse optoelectronic devices. However, their charge transport properties remain elusive, plagued by the issues of excessive contact resistance and large hysteresis in ambient conditions. Here we report a van der Waals integration approach for creating high-performance contacts on monocrystalline halide perovskite thin films with minimum interfacial damage and an atomically clean interface. Compared to the deposited contacts, our van der Waals contacts exhibit two to three orders of magnitude lower contact resistance, enabling systematic transport studies in a wide temperature range. We report a Hall mobility exceeding 2,000 $cm^2 V^{-1} s^{-1}$ at around 80 K, an ultralow bimolecular recombination coefficient of 3.5×10^{-15} $cm^3 s^{-1}$ and a photocurrent gain $>10^6$ in the perovskite thin films. Furthermore, magnetotransport studies reveal a quantum-interference-induced weak localization behaviour with a phase coherence length up to 49 nm at 3.5 K. Our results lay the foundation for exploring new physics in this class of 'soft-lattice' materials.

Despite the considerable potential of halide perovskites for high-performance photovoltaics[1], light emitting diodes (LEDs)[2] and radiation detection devices[3], the fundamental understanding of their charge transport properties is lagging, largely due to the difficulties in forming high-quality electrical contacts. In particular, the halide perovskites are generally soluble in various solvents and incompatible with typical lithography processes, and they are highly delicate and prone to degradation during conventional vacuum metal deposition processes[4,5]. Thus, it remains a standing challenge to use conventional lithography to create reliable electrical contacts to halide perovskites, and the intrinsic electrical transport properties are often seriously convoluted and plagued by poor electrical contacts (typically with a contact resistance, R_c, three orders of magnitude larger than the intrinsic material resistance). Additionally, halide perovskites feature an ionic 'soft-lattice' (ref. [6]), with considerable ion movement and current drift at room temperature, which further complicates the accurate measurement and analysis of the fundamental transport properties.

For example, the space charge limited current (SCLC) model is frequently used for evaluating the mobility and trap density of various perovskites. However, non-ideal contacts and well-known current–voltage (I–V) hysteresis could seriously compromise its accuracy and the relevant derivations. Additionally, this approach is not applicable for probing photocarrier dynamics that are critical for optoelectronic devices[7]. Non-contact spectroscopic techniques have been explored to probe the basic charge carrier behaviour but only give an indirect evaluation of local carrier dynamics and often require complex mathematical modelling and derivations[8]. Hall measurements represent the most direct method for probing charge carrier behaviour, with minimum derivations and reduced uncertainties, and are commonly used for the evaluation of most conventional semiconductors such as Si (ref. [9]) and GaAs (ref. [10]). Despite some pioneering efforts in the Hall measurement of perovskite materials with electrodes defined by shadow-mask evaporation, these studies are often complicated and sometimes dictated by the excessive R_c, raising uncertainties on the accuracy[11,12]. In general, a reasonably low R_c and a small R_c variation (δR_c) are strictly required for accurately determining the intrinsic material resistance (R_{xx}) and Hall resistance (R_{xy}; Supplementary Fig. 1). Furthermore, measurements at cryogenic temperatures that can reduce or even completely freeze the ion movement are highly desired[6]. However, the quality of electrical contacts usually degrades rapidly with decreasing temperature[13]. Therefore, for reliable measurement, it is critical to create high-quality contacts that can sustain cryogenic conditions with reasonably low R_c.

Herein, we report a systematic investigation of the long-range photocarrier transport properties of vapour-phase-grown monocrystalline lead halide perovskite thin films by exploiting high-quality van der Waals contacts (vdW-contacts)[14,15]. Transport studies with vdW-contacts show linear I–V characteristics at both room temperature and cryogenic temperature, with R_c two to three orders of magnitude lower than that of the deposited contacts throughout the measurement temperature regime. The temperature-dependent transport studies reveal a highest carrier mobility exceeding 2,000 $cm^2 V^{-1} s^{-1}$ at around 80 K, an ultralow bimolecular recombination coefficient of 3.5×10^{-15} $cm^3 s^{-1}$ at room temperature and a photocurrent gain of 10^6–10^7 in perovskite thin films. Furthermore, magnetotransport

[1]Department of Chemistry and Biochemistry, University of California, Los Angeles, CA, USA. [2]State Key Laboratory for Chemo/Biosensing and Chemometrics, College of Chemistry and Chemical Engineering, Hunan University, Changsha, China. [3]Department of Materials Science and Engineering, University of California, Los Angeles, CA, USA. [4]Beijing Advanced Innovation Center for Materials Genome Engineering, Beijing Key Laboratory for Advanced Energy Materials and Technologies, University of Science and Technology Beijing, Beijing, China. [5]Sustainable Energy Technologies Centre, College of Engineering, King Saud University, Riyadh, Kingdom of Saudi Arabia. [6]These authors contributed equally: Yiliu Wang, Zhong Wan, Qi Qian. ✉e-mail: xduan@chem.ucla.edu

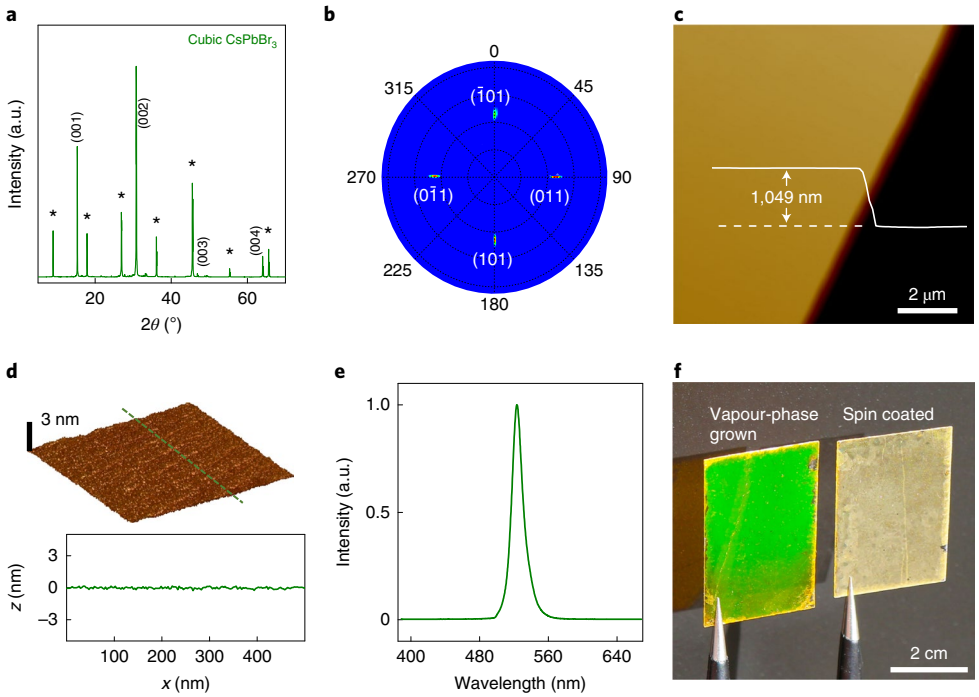

Fig. 1 | Characterization of monocrystalline $CsPbBr_3$ thin film. a, X-ray diffraction pattern of the $CsPbBr_3$ thin film grown on muscovite shows only (00*l*) planes, suggesting highly oriented growth. Peaks from the muscovite substrate monoclinic phase (JCPDS no. 00-002-0056) with the (001) plane exposed are marked *. **b**, The (110) pole figure of the $CsPbBr_3$ thin film showing four poles with equal intervals corresponding to symmetrical planes of the {110} family. **c**, Large-area AFM image of the as-grown film, with the line profile showing the thickness of the film. **d**, A 3D image of the surface topography of the $CsPbBr_3$ thin film (upper) with the corresponding line profile plot (lower), highlighting an ultra-smooth surface with a small root mean square roughness of 0.19 nm. **e**, Photoluminescence emission spectrum of the $CsPbBr_3$ thin film. **f**, Photograph of the as-grown $CsPbBr_3$ thin film (left) and spin-coated thin film (right) under direct sunlight illumination (2:00 p.m. in Los Angeles). The size of the as-grown $CsPbBr_3$ thin film can be readily scaled up to the multi-centimetre scale, and is only limited by the inner diameter of the quartz tube of the CVD system. Some non-uniformity seen in the photograph is attributed to the long-range unevenness of the exfoliated muscovite substrate (with slightly different scattering at different angles) and accidental scratches when handling with tweezers, instead of the intrinsic optical quality of the material.

studies below 20 K reveal a quantum-interference-induced weak localization behaviour in halide perovskites with a phase coherence length up to 49 nm at 3.5 K, comparable to black phosphorus or InSe at a similar carrier density[16,17].

Van der Waals contacts on perovskites

The $CsPbBr_3$ perovskite thin film was directly grown on the freshly exfoliated (001) surface of the muscovite substrate at ~500 °C in a home-built chemical vapour deposition (CVD) system. X-ray diffraction studies display only the (00*l*) planes of the cubic phase $CsPbBr_3$ (JCPDS no. 00-054-0752; Fig. 1a), suggesting a highly oriented thin film growth with the (001) plane of $CsPbBr_3$ in parallel to the (001) plane of the muscovite substrate. The in-plane orientation of the film over the centimetre scale was evaluated with parallel beam reflection diffraction studies. The resulting (110) pole figure shows four symmetrical poles with a 90° interval corresponding to the four equivalent {110} family planes (Fig. 1b), confirming the single-crystalline nature of the resulting thin film.

Atomic force microscopy (AFM) studies show that the resulting thin film exhibits a film thickness of ~1 μm (Fig. 1c) and reveal that the surface is nearly atomically flat, with a root mean square roughness of ~0.19 nm (Fig. 1d), which is essential for ensuring an intimate contacting interface with the laminated electrodes to enable the formation of high-quality vdW-contacts.

Photoluminescence studies show a single emission peak at about 530 nm (Fig. 1e), consistent with the band-edge emission in $CsPbBr_3$ (ref. [18]). Notably, the as-grown film under direct sunlight shows a bright green light emission over the entire substrate, while the spin-coated $CsPbBr_3$ thin film does not show apparent green emission under the same condition (Fig. 1f). The bright green light emission under natural sunlight illumination without an optical filter suggests that the emission dominates the reflection, absorption or scattering of the white light, which gives a direct visual indication of the high optical quality of the film[19].

To fabricate high-quality electrical contacts, we adopted a vdW-integration approach[14] (see Fig. 2a and Methods), where the prefabricated, atomically flat thin film gold electrodes are laminated onto the large-area perovskite thin films (Fig. 2b,c) without directly exposing the perovskites to any lithography or deposition steps. For comparison, we also fabricated electrodes of the same geometry using a conventional vacuum deposition process (see Methods). Photoluminescence images of the devices show little emission in the area covered by the metal electrode for both the deposited contacts (Fig. 2d) and vdW-contacts (Fig. 2f) due to the blockage of the light by the Au electrodes. We next tried to peel off the electrodes to expose the underlying perovskite for photoluminescence studies. Apparently, the vdW-contacts can be readily peeled off due to the nature of the weak vdW interaction (Fig. 2g), while it is much more difficult to peel off the deposited contacts (with a much lower peeling-off yield) (Fig. 2e), suggesting a much stronger bonding between the perovskites and the deposited contacts. Notably, in the case where the deposited contacts did get peeled off, little photoluminescence emission was observed in the area that was initially covered by the deposited electrodes, even though there was no apparent

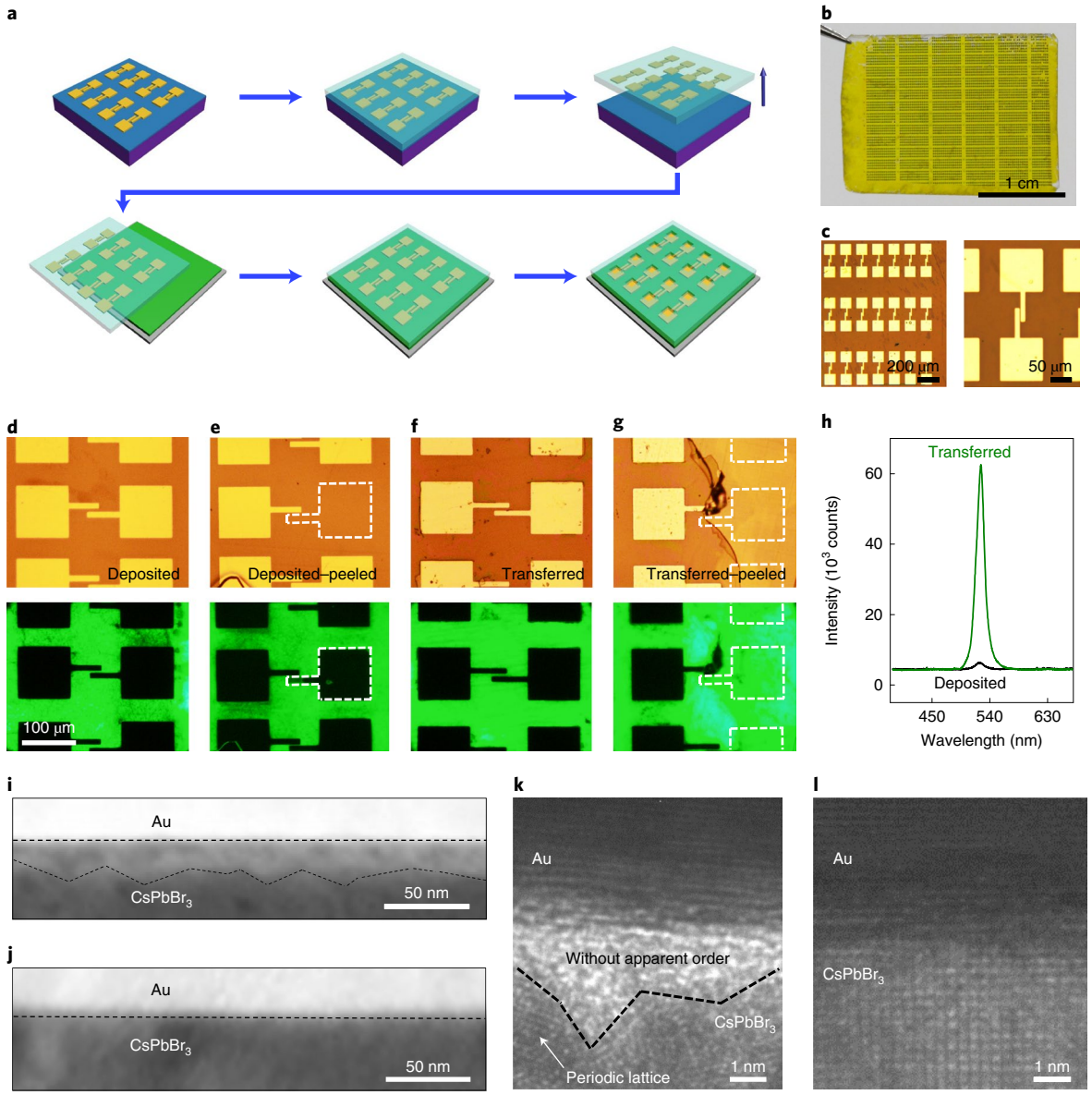

Fig. 2 | Formation of damage-free vdW-contacts by transfer approach. a, Schematic diagram for the transfer contact approach. **b**, Photograph of transferred electrode arrays on the entire substrate, allowing the scalable integration of electrode arrays on perovskite thin films over the entire centimetre-scale substrate. **c**, Photograph of Au electrode arrays transferred on perovskite thin film, and close-up image of a two-terminal device with a 2 μm channel. **d**,**e**, Photograph (upper panel) and photoluminescence images (lower panel) of deposited electrodes on perovskite thin film before (**d**) and after (**e**) the electrodes were peeled off (exposed area outlined by the white dashed lines). **f**,**g**, Photograph and photoluminescence images of transferred electrodes on perovskite thin film before (**f**) and after (**g**) the electrodes were peeled off (exposed area outlined by the white dashed lines). **h**, Photoluminescence emission spectra from the areas where deposited (black) and transferred (green) electrodes were peeled. **i**,**j**, Scanning transmission electron microscopy images of the cross-section of the $CsPbBr_3$ thin film with the deposited electrodes (**i**) and vdW electrodes (**j**). The deposited interface shows an additional heterogeneous interfacial layer highlighted by the dashed zigzag lines, and the vdW-contact shows a straight interface. **k**,**l**, High-resolution transmission electron microscopy images of the cross-section of the $CsPbBr_3$ thin film with the deposited electrodes showing a disordered interface (partly polycrystalline and partly amorphous, as suggested by the area without apparent order) under the electrodes (**k**), and the transferred electrodes showing atomically sharp interfaces (**l**).

optical contrast with the surrounding area that was not covered by the deposited electrode, suggesting the underlying perovskite is seriously damaged by the metal deposition process. By contrast, for the area covered by the transferred vdW-contacts, the photoluminescence is essentially unchanged after removing the electrodes (Fig. 2g), suggesting that the vdW-contact approach is essentially damage-free, which is also demonstrated in the corresponding photoluminescence spectra (Fig. 2h).

The cross-sectional scanning transmission electron microscopy image of the interface with deposited gold shows a zigzag heterogeneous interfacial layer (~20–30 nm thick; Fig. 2i), while the interface with the transferred electrode shows a straight, sharp interface (Fig. 2j). The high-resolution transmission electron microscopy studies further confirm the deposited interface is highly disordered, while the vdW interface shows an atomically clean and atomically sharp transition from the Au lattice to the perovskite lattice with no

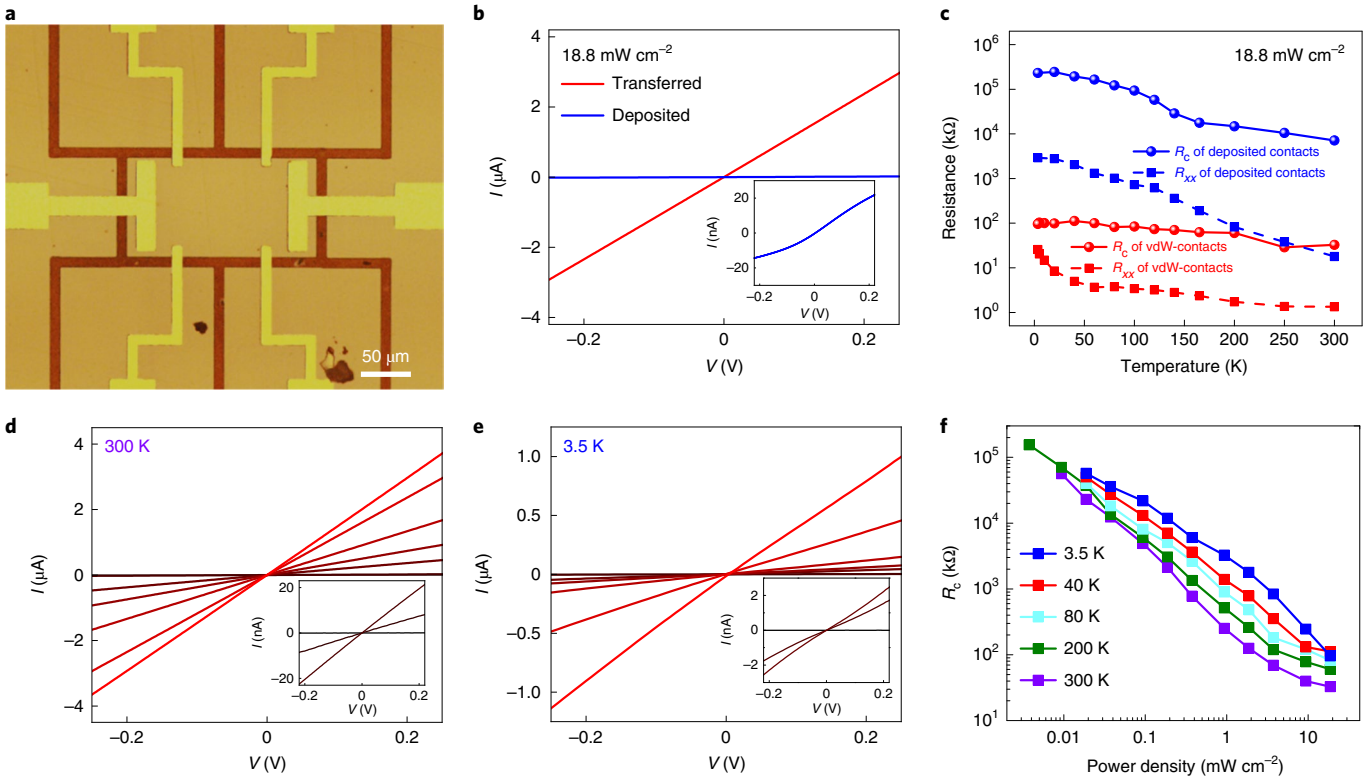

Fig. 3 | Performance of the vdW-contacts. a, Photograph of a typical Hall bar device prepared by the vdW-contact approach; for comparison, we have also prepared parallel devices of identical geometry with deposited electrodes. **b**, Room temperature *I*–*V* of the devices with deposited (blue) and vdW (red) contacts under a blue LED illumination power density of 18.8 mW cm^{-2}. Inset: close-up *I*–*V* plots for the device with deposited contacts. **c**, Comparison of the contact (dot) and channel (square) resistance of the devices with deposited contacts and vdW-contacts at various temperatures; the channel resistance R_{xx} was obtained using four-probe measurements with the standard Hall bar device, and the contact resistance was then calculated by subtracting the channel resistance (R_{xx}) from the two-terminal resistance (d*V*/d*I* near zero voltage). **d**,**e**, *I*–*V* characteristics of the vdW-contacted device at room temperature (**d**) and 3.5 K (**e**) under various illumination intensities; the power density for each curve (from black to red) is 0, 0.01, 0.1, 0.9, 1.9, 3.8, 9.4 and 18.8 mW cm^{-2}. Insets: close-up *I*–*V* plots under 0, 0.01 and 0.1 mW cm^{-2} illumination. **f**, Illumination-power-dependent contact resistance of the vdW-contacts at different temperatures. Here, the R_{xx} measurements were conducted with an illumination power above 0.003 mW cm^{-2} to ensure a more reliable evaluation of the photocarrier transport characteristics.

apparent impurities or disorder in between (Fig. 2k,l). These studies clearly demonstrate that the vdW-integration approach offers a damage-free metal-integration process.

Contact resistance

We fabricated standard Hall bar devices (Fig. 3a) for basic two-terminal and four-terminal *I*–*V* measurements to evaluate the contact resistance (R_c) and intrinsic materials resistance (R_{xx}). Control devices with deposited electrodes were also fabricated for comparison. The perovskite devices usually exhibit a rather high two-terminal resistance on the order of gigaohms at room temperature that rapidly increases to ~100 GΩ at lower temperatures in the dark (Supplementary Fig. 2a,b), which exceeds the internal impedance of typical voltmeters and makes it highly unreliable to perform accurate four-terminal measurement to decouple R_c and R_{xx} (Supplementary Fig. 1). Therefore, to reduce the measurement error over a wide temperature range and allow a reliable analysis of carrier dynamics over different carrier concentration regimes, we used variable light illumination to tune the carrier density in the material.

Under a blue LED illumination at 18.8 mW cm^{-2}, the device with deposited contacts shows non-linear *I*–*V* behaviour with a typical two-terminal sheet resistance >20 MΩ□$^{-1}$ at 300 K (blue curve in Fig. 3b), which is largely consistent with previous studies (Supplementary Table 2). By contrast, the device with vdW-contacts exhibits linear *I*–*V* behaviour under the same conditions with the two-terminal sheet resistance on the order of 100 kΩ□$^{-1}$ (red curve in Fig. 3b), about two orders of magnitude lower. The much higher apparent sheet resistance observed in the same material with deposited contacts suggests the charge transport in such devices is dictated by R_c rather than R_{xx}.

The R_c for the deposited contact is on the order of 10–100 MΩ, while that for the vdW-contact is on the order of 100 kΩ (Fig. 3c). Throughout the entire measurement regime, the R_c of vdW-contacted devices is approximately two to three orders of magnitude lower than that of the deposited contacts, which may be largely attributed to the atomically clean interface at the vdW-contacts[14,15]. The R_{xx} values measured from the devices with vdW-contacts or deposited contacts show a similar trend with temperature, but with the R_{xx} value determined from deposited contacts more than ten times larger (Fig. 3c), which might be partly attributed to deposition-induced material damage beyond the direct contacting region (as also indicated by the dark streaks between contact pads observed in the photoluminescence images in Fig. 2d,e) as well as uncertainties due to excessive R_c in the deposited contacts (Supplementary Fig. 1). Notably, the measured R_{xx} (1–100 kΩ for a device with a channel length of 150 μm) is much lower than R_c (Fig. 3c), further confirming that the typical two-terminal transport is dictated by the R_c, especially in the samples with deposited contacts.

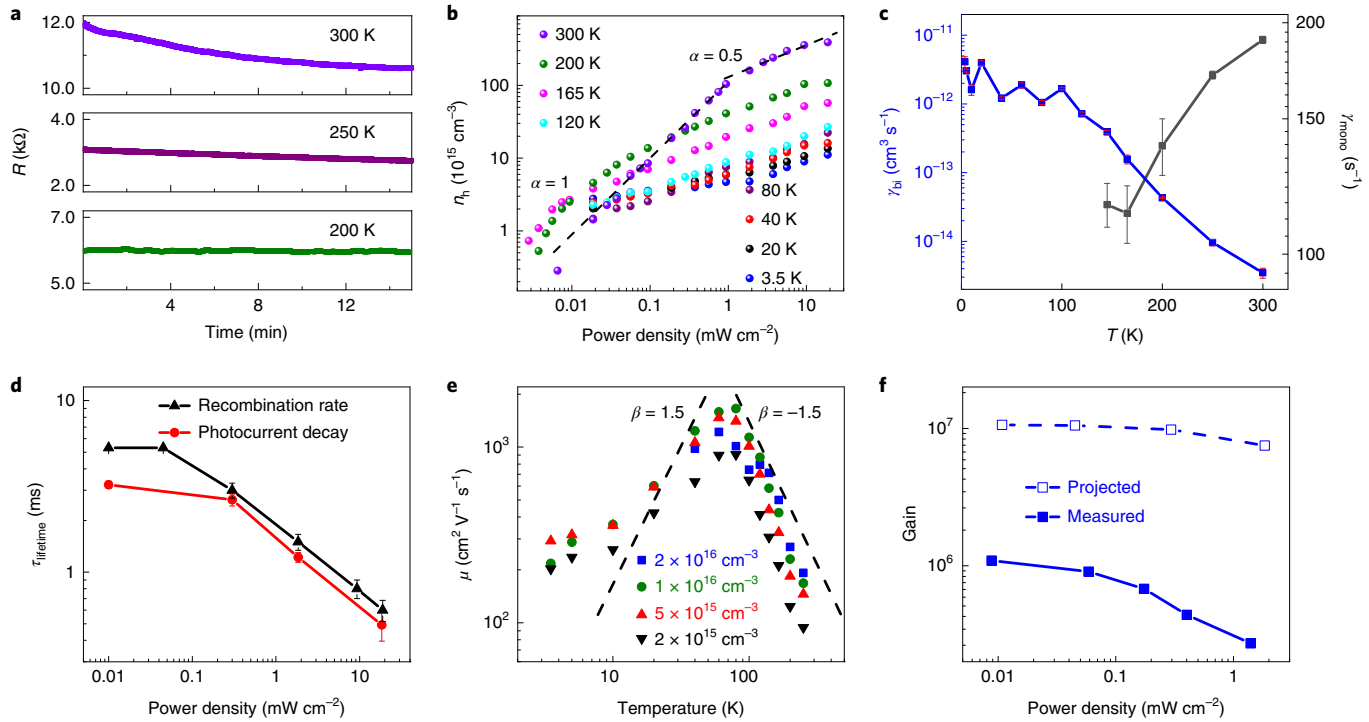

Fig. 4 | Electrically probing the photocarrier dynamics of perovskites using vdW-contacts. a, Resistance drift at different temperatures, highlighting the considerable resistance drift due to bias-induced ion movements at room temperature, which can be completely frozen out with no drift below 200 K. **b**, Illumination-power-dependent carrier density n_h at different temperatures; the dashed lines follow P and $P^{0.5}$. **c**, The extracted temperature-dependent monomolecular (black) and bimolecular (blue) electron–hole recombination coefficient from **b**. **d**, Comparison between the carrier recombination lifetime determined from direct transient photocurrent measurement and that extracted from the recombination coefficient in **c**; the error bars in **c** and **d** are from fitting uncertainties. **e**, Hall mobility as a function of temperature at different carrier densities. The dashed lines follow $T^{1.5}$ and $T^{-1.5}$. The Hall measurement gives a carrier density of 4.8×10^{13} cm^{-3} and mobility of 7.5 cm^2 V^{-1} s^{-1} under dark conditions at room temperature. **f**, Photocurrent gain values of a two-terminal photoconductor device with 2 μm channel length. The projected results were calculated using $\tau_{lifetime}/\tau_{transit}$ and are plotted in the dashed line and compared with the measured gain.

To further evaluate the quality of the vdW-contacts, the illumination-intensity-dependent I–V were collected from 18.8 mW cm^{-2} to completely dark. The I–V remains linear at all illumination conditions at room temperature (Fig. 3d and Supplementary Fig. 2a). Temperature-dependent studies further show that linear I–V characteristics persist even at 3.5 K (Fig. 3e). Across measurement temperatures, R_c decreases with increasing illumination power (Fig. 3f), indicating the importance of carrier generation for reducing R_c. At a fixed illumination power density, R_c increases monotonically with decreasing temperature (Supplementary Fig. 2c), which might be attributed to reduced carrier injection efficiency across the contact interface at lower temperature[13].

Photocarrier dynamics probed with van der Waals contacts

To conduct reliable Hall measurements, it is critical to maintain a stable sample condition during the magnetic field sweeping process, which is particularly challenging for halide perovskites due to considerable bias-induced ion movement and current drift over time. To this end, we first monitored sample resistance drift versus time at different temperatures (Fig. 4a). Expectedly, there is a large R_{xx} drift at 300 K, which can be suppressed at lower temperature and essentially vanishes below 200 K.

To minimize bias-induced drift during the relatively long time duration needed to sweep the magnetic field in a typical Hall measurement, we used transient Hall measurement to derive the carrier density at room temperature (Supplementary Fig. 3a–d). When resistance drift is eliminated below 200 K, we can conduct the standard Hall measurements with sweeping magnetic field (Supplementary Fig. 3e). Our analyses indicate that the transport is dominated by holes (see Methods and Supplementary Fig. 3e,f), with carrier concentration (n_h) increasing with increasing illumination power density (P), following $n_h \propto \frac{P}{\gamma_{mono}}$ in the low-illumination regime (for example, $P < 1$ mW cm^{-2} at room temperature) where the trap-assisted electron–hole recombination dominates, and $n_h \propto \left(\frac{P}{\gamma_{bi}}\right)^{0.5}$ in the high-illumination regime, where band-to-band electron–hole recombination dominates (Fig. 4b)[11]; γ_{mono} and γ_{bi} represent the monomolecular and bimolecular recombination coefficients, respectively.

The γ_{mono} and γ_{bi} coefficients show distinct temperature dependence (Fig. 4c). The γ_{mono} value becomes smaller at lower temperature, suggesting a reduced monomolecular recombination probability when the kinetic energy is suppressed. The transition point of the monomolecular to bimolecular recombination regime moves to a lower illumination power density with decreasing temperature. Below 140 K, bimolecular recombination dominates the whole measurement range. The γ_{bi} value increases monotonically with decreasing temperature (see Supplementary Fig. 4 for fitting details). This trend cannot be simply explained by the previously suggested mobility-dependent picture[20] or the spin-split indirect band picture[21], although we cannot totally rule out the possibility of the latter, which will be an interesting topic for further investigation. It has been proposed that electrons and holes are dressed in phonon excitations in the 'soft-lattice' halide perovskites, forming polarons[22,23]. Since electron polarons and hole polarons have different effects on structural bending, it is energetically more favourable if

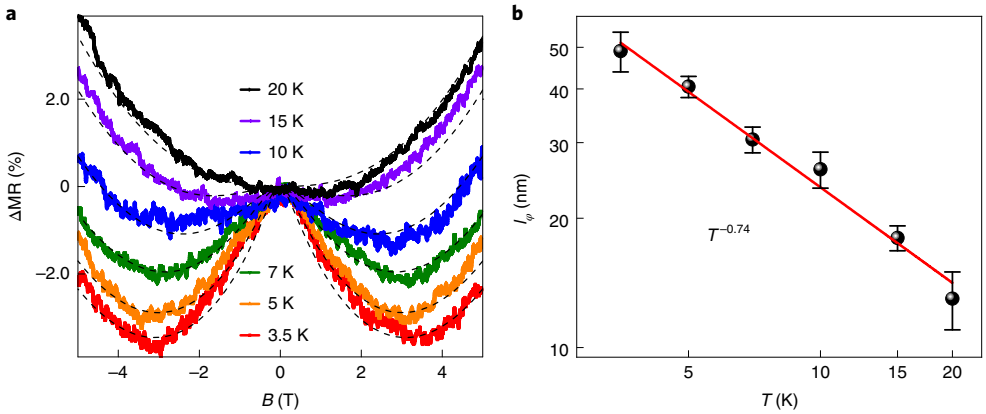

Fig. 5 | Magnetoresistance at the lowest temperatures. a, The weak localization signal from 20 K to 3.5 K; $\Delta MR = (R_{xx} - R_{xx,B=0T})/R_{xx,B=0T}$. The dashed lines are fitting at each temperature. **b**, Phase coherence length as a function of temperature. The error bars are from the MR fitting uncertainties, and the red line is the linear fit of l_φ versus $1/T$.

they are spatially separated. Therefore, a spacing must be overcome before they recombine, which could considerably slow the bimolecular recombination rate[6,24]. Indeed, a γ_{bi} as low as 3.5×10^{-15} cm^3 s^{-1} is obtained at room temperature, which is about five orders of magnitude lower than that of typical direct bandgap semiconductors (for example, ~10^{-10} cm^3 s^{-1} in GaAs) and nearly comparable to that in indirect bandgap semiconductors (10^{-14}–10^{-15} cm^3 s^{-1} in Si and Ge). The reduced carrier–phonon coupling at low temperature weakens the polaronic effect and hence increases the bimolecular recombination rate. Such a picture is consistent with our observed temperature-dependent trend (Fig. 4c, blue line). Additionally, this γ_{bi} is also about two to four orders of magnitude lower than that reported in hybrid perovskite ($MAPbBr_3$)[25,26]. We suspect it might be attributed to the stronger structural bending in all-inorganic perovskites than in hybrid perovskites, as suggested in a previous theory[24], which could lead to a stronger polaron protection effect to further lower the bimolecular recombination rate.

Based on γ_{mono} and γ_{bi}, we further extracted the carrier recombination lifetime ($\tau_{lifetime}$; see Methods). The $\tau_{lifetime}$ decreases from 5.3 ms to 0.6 ms as the illumination power density increases from 0.01 mW cm^{-2} to 18.8 mW cm^{-2}, which is consistent with a previous study[27] and with the $\tau_{lifetime}$ directly determined from transient photocurrent measurements (Fig. 4d and Supplementary Fig. 5).

The carrier mobility was derived at various temperatures and illumination intensities. Under proper illumination power, our measurement gives a highest room temperature Hall mobility of 118 cm^2 V^{-1} s^{-1}, which increases up to 1,650 cm^2 V^{-1} s^{-1} at 80 K (Fig. 4e and Supplementary Fig. 6). At each temperature, the mobility first increases with the increasing illumination power, which occurs because the larger carrier density increases the Fermi wave vector, therefore leading to a larger change of momentum in the scattering process, and a reduced back-scattering probability[28]. On the other hand, as density further increases, the carrier–carrier interaction starts to play a dominant role, leading to reduced mobility under even stronger illumination conditions (Supplementary Fig. 6)[29]. The highest mobility achieved among all the measured samples is 2,080 cm^2 V^{-1} s^{-1} at 80 K (sample B in Supplementary Fig. 7). We also conducted transport studies in large devices (up to 0.5 cm long), and obtained largely consistent results (Supplementary Fig. 8).

At a given carrier density, the mobility versus temperature relationship above ~80 K follows a negative power law: $\mu \propto T^{-\beta}$ with $\beta \approx 1.46$ (Fig. 4e). This power law is consistent with the classical theory of acoustic phonon–electron scattering dominated scheme, where $\mu \propto T^{-1.5}$ is expected[13]; however, the theoretically predicted room-temperature mobility within this picture exceeds 1,000 cm^2 V^{-1} s^{-1} in $MAPbI_3$[30,31] and $MASnI_3$ perovskites[32,33], while our highest mobility measured at room temperature is 118 cm^2 V^{-1} s^{-1}. On the other hand, the negative scaling law can also be explained by the formation of large polarons in halide perovskite[6]. In particular, the polaronic effect involving acoustic phonons would also give the same $T^{-1.5}$ scaling behaviour, but with a much lower mobility value predicted due to increased electron–phonon interaction and increased effective mass (10 cm^2 V^{-1} s^{-1} at 300 K and 150 cm^2 V^{-1} s^{-1} at 100 K)[34]. Nonetheless, the exact calculated mobility value could vary substantially depending on the effective mass and assumed impurity density used in the calculation. By considering the polaronic effect involving polar-optical phonons, theoretical studies predict a $T^{-0.5}$ scaling relationship above 100 K but with an increased power factor at lower temperature[35]; thus, we cannot completely exclude the polar-optical phonon scattering model simply based on the temperature scaling behaviour. Below 80 K, the mobility decreases with decreasing temperature at all illumination conditions, which indicates the possibility that the classical impurity scattering process dominates the back-scattering-related transport in this temperature regime[13]. A temperature-dependent phase transition could also contribute to mobility temperature dependence, which is typically manifested as an abrupt change of mobility[34], but not obvious in our study.

With the unique combination of long $\tau_{lifetime}$ and high μ, the perovskite thin films exhibit an unusually large value of the product $\tau_{lifetime}\mu$ and thus offer the material foundation for an exceptionally high photocurrent gain in a photoconductor as determined by the following:

$$G = \frac{\tau_{lifetime}}{\tau_{transit}} = \frac{\tau_{lifetime}\mu V}{L^2} \quad (1)$$

where V is the bias voltage and L is the channel length (see Methods). To further push the limit of the photocurrent gain, it is necessary to shorten the channel length and reduce the transit time, which has been difficult to achieve in halide perovskite due to its incompatibility with the typical lithography processes that are necessary for creating high-resolution devices. To this end, we fabricated a two-terminal device with a 2 μm channel length and studied its photoresponse characteristics (Supplementary Fig. 9). Based on the lifetime and mobility obtained from Hall measurements, we can project the upper limit of the photocurrent gain based on the device geometry using equation (1) (dashed line in Fig. 4f). The projected photocurrent gain exceeds 10^7 at a 2 V bias, and decreases with increasing illumination power density.

Remarkably, the experimentally measured photocurrent gain as derived using equation (10) in Methods shows a similar trend (solid line in Fig. 4f), with a highest gain of 1.2×10^6 achieved at a 2 V bias and 0.01 mW cm^{-2} illumination. Our measured photocurrent gain values are about one order of magnitude smaller than the projected ones. This difference occurs because our calculation assumes a 2 V bias drop entirely on the channel, while the actual voltage drop is much smaller due to the considerable R_c. The difference between the projected and measured gain values becomes smaller at lower illumination, which may be partly attributed to the higher R_{xx}/R_c ratio at lower illumination. By further reducing the illumination, an even higher gain of 8.7×10^6 is achieved (Supplementary Fig. 9). This analysis demonstrates that the gain may be further improved by continuing to optimize the contact.

Magnetotransport properties and weak localization effect

Reliable vdW-contacts down to the base temperature allow us to conduct magnetoresistance (MR) studies and probe the quantum transport properties in the perovskite (Fig. 5a). At $T=3.5$ K, the device shows a negative MR at a low field, which switches to a positive MR at a higher field. The higher resistance at the zero field can be attributed to a quantum-interference-induced weak localization effect: the constructive interference of backscattered electronic wave functions increases the probability of localizing an electron and hence a higher resistance at zero magnetic field[36], while the presence of a magnetic field breaks the phase coherence and such an interference effect, leading to a reduced resistance and negative MR. This feature becomes less apparent with increasing temperature and disappears above 20 K, as the phase coherence length l_φ becomes comparable to the mean free path l_μ.

Based on the MR data, we can extract a phase coherence length l_φ at each temperature (see Methods and Fig. 5b), which yields l_φ values of 49 nm and 12 nm at 3.5 K and 20 K, respectively. Remarkably, we found that those length scales are comparable to those of the covalent two-dimensional (2D) semiconductors such as black phosphorus or InSe at a similar carrier density, suggesting that the electronic quality of the ionic 'soft-lattice' perovskites is nearly comparable to that of the high-quality 2D semiconductors. The l_φ versus temperature follows $l_\varphi \approx T^{-0.74}$, in good agreement with the localization theory in the three-dimensional (3D) system (where a −0.75 power law dependence is expected[37]) and indicating that the carrier–carrier interaction dominates the phase coherence behaviour. However, in our measurement regime, we did not observe the weak anti-localization effect predicted in perovskite[38]. It is likely that the spin–orbital coherence length l_{so} is always greater than l_φ throughout our measurement regime.

Conclusions

Enabled by high-quality vdW-contacts, the robust observation of high Hall mobility and a quantum-interference-induced weak localization effect in 'soft-lattice' ionic halide perovskites is exciting, and suggests perovskites as a unique material platform for fundamental transport studies and the exploration of new physics beyond conventional covalent semiconductors. The damage-free integration of metal contacts on delicate halide perovskites may be extended to create other functional contacts (for example, a ferromagnetic or superconducting metal contact) with a highly transparent interface, and enable probing other exotic properties in halide perovskites. Beyond their use in high-performance photovoltaics and LEDs, halide perovskites have been suggested to exhibit many other attractive attributes. For example, they have a giant spin–orbit coupling that can be used for spintronics[39]. However, despite the exciting prospects from optical studies, the relevant transport studies to date have been largely plagued by poor contacts. The ability to make high-quality contacts is critical for reliable spin transport studies to fully unlock the potential of this unique class of materials. This vdW-integration approach is also generally applicable for various delicate materials, including organic crystals and molecular monolayers, and opens up exciting opportunities to explore these unconventional electronic materials for both fundamental studies and high-performance devices.

Online content

Any methods, additional references, Nature Research reporting summaries, source data, extended data, supplementary information, acknowledgements, peer review information; details of author contributions and competing interests; and statements of data and code availability are available at https://doi.org/10.1038/s41565-020-0729-y.

Received: 2 December 2019; Accepted: 3 June 2020;
Published online: 13 July 2020

References

1. Nie, W. et al. High-efficiency solution-processed perovskite solar cells with millimeter-scale grains. *Science* **347**, 522–525 (2015).
2. Cao, Y. et al. Perovskite light-emitting diodes based on spontaneously formed submicrometre-scale structures. *Nature* **562**, 249–253 (2018).
3. Fang, Y., Dong, Q., Shao, Y., Yuan, Y. & Huang, J. Highly narrowband perovskite single-crystal photodetectors enabled by surface-charge recombination. *Nat. Photonics* **9**, 679–686 (2015).
4. Spicer, W., Chye, P., Garner, C., Lindau, I. & Pianetta, P. The surface electronic structure of 3–5 compounds and the mechanism of Fermi level pinning by oxygen (passivation) and metals (Schottky barriers). *Surf. Sci.* **86**, 763–788 (1979).
5. Haick, H., Ambrico, M., Ghabboun, J., Ligonzo, T. & Cahen, D. Contacting organic molecules by metal evaporation. *Phys. Chem. Chem. Phys.* **6**, 4538–4541 (2004).
6. Miyata, K., Atallah, T. L. & Zhu, X. Lead halide perovskites: crystal-liquid duality, phonon glass electron crystals, and large polaron formation. *Sci. Adv.* **3**, e1701469 (2017).
7. Mott, N. F. & Gurney, R. W. *Electronic Processes in Ionic Crystals* (Oxford Univeristy Press, 1940).
8. Herz, L. M. Charge-carrier mobilities in metal halide perovskites: fundamental mechanisms and limits. *ACS Energy Lett.* **2**, 1539–1548 (2017).
9. Green, M. A. Intrinsic concentration, effective densities of states, and effective mass in silicon. *J. Appl. Phys.* **67**, 2944–2954 (1990).
10. Manfra, M. J. Molecular beam epitaxy of ultra-high-quality AlGaAs/GaAs heterostructures: enabling physics in low-dimensional electronic systems. *Annu. Rev. Condens. Matter Phys.* **5**, 347–373 (2014).
11. Chen, Y. et al. Extended carrier lifetimes and diffusion in hybrid perovskites revealed by Hall effect and photoconductivity measurements. *Nat. Commun.* **7**, 12253 (2016).
12. Yi, H. T., Wu, X., Zhu, X. & Podzorov, V. Intrinsic charge transport across phase transitions in hybrid organo-inorganic perovskites. *Adv. Mater.* **28**, 6509–6514 (2016).
13. Sze, S. M. & Ng, K. K. *Physics of Semiconductor Devices*. (Wiley, 2006).
14. Liu, Y. et al. Approaching the Schottky–Mott limit in van der Waals metal–semiconductor junctions. *Nature* **557**, 696–700 (2018).
15. Liu, Y., Huang, Y. & Duan, X. Van der Waals integration before and beyond two-dimensional materials. *Nature* **567**, 323–333 (2019).
16. Du, Y., Neal, A. T., Zhou, H. & Peide, D. Y. Weak localization in few-layer black phosphorus. *2D Mater.* **3**, 024003 (2016).
17. Zeng, J. et al. Gate-tunable weak antilocalization in a few-layer InSe. *Phys. Rev. B* **98**, 125414 (2018).
18. Eaton, S. W. et al. Lasing in robust cesium lead halide perovskite nanowires. *Proc. Natl Acad. Sci. USA* **113**, 1993–1998 (2016).
19. Imran, M. et al. Simultaneous cationic and anionic ligand exchange for colloidally stable $CsPbBr_3$ nanocrystals. *ACS Energy Lett.* **4**, 819–824 (2019).
20. Milot, R. L., Eperon, G. E., Snaith, H. J., Johnston, M. B. & Herz, L. M. Temperature-dependent charge-carrier dynamics in $CH_3NH_3PbI_3$ perovskite thin films. *Adv. Funct. Mater.* **25**, 6218–6227 (2015).
21. Azarhoosh, P. et al. Research update: Relativistic origin of slow electron-hole recombination in hybrid halide perovskite solar cells. *APL Mater.* **4**, 091501 (2016).
22. Zhu, X. & Podzorov, V. Charge carriers in hybrid organic-inorganic lead halide perovskites might be protected as large polarons. *J. Phys. Chem. Lett.* **6**, 4758–4761 (2015).
23. Zhu, H. et al. Screening in crystalline liquids protects energetic carriers in hybrid perovskites. *Science* **353**, 1409–1413 (2016).
24. Miyata, K. et al. Large polarons in lead halide perovskites. *Sci. Adv.* **3**, e1701217 (2017).

25. Oga, H., Saeki, A., Ogomi, Y., Hayase, S. & Seki, S. Improved understanding of the electronic and energetic landscapes of perovskite solar cells: high local charge carrier mobility, reduced recombination, and extremely shallow traps. *J. Am. Chem. Soc.* **136**, 13818–13825 (2014).
26. Wehrenfennig, C., Liu, M., Snaith, H. J., Johnston, M. B. & Herz, L. M. Charge-carrier dynamics in vapour-deposited films of the organolead halide perovskite $CH_3NH_3PbI_{3-x}Cl_x$. *Energy Environ. Sci.* **7**, 2269–2275 (2014).
27. Dong, Q. et al. Electron-hole diffusion lengths > 175 μm in solution-grown $CH_3NH_3PbI_3$ single crystals. *Science* **347**, 967–970 (2015).
28. Ihn, T. *Semiconductor Nanostructures: Quantum States and Electronic Transport* (Oxford University Press, 2010).
29. Hendry, E., Koeberg, M., Pijpers, J. & Bonn, M. Reduction of carrier mobility in semiconductors caused by charge-charge interactions. *Phys. Rev. B* **75**, 233202 (2007).
30. Zhao, T., Shi, W., Xi, J., Wang, D. & Shuai, Z. Intrinsic and extrinsic charge transport in $CH_3NH_3PbI_3$ perovskites predicted from first-principles. *Sci. Rep.* **6**, 19968 (2016).
31. Mante, P. A., Stoumpos, C. C., Kanatzidis, M. G. & Yartsev, A. Electron–acoustic phonon coupling in single crystal $CH_3NH_3PbI_3$ perovskites revealed by coherent acoustic phonons. *Nat. Commun.* **8**, 14398 (2017).
32. He, Y. & Galli, G. Perovskites for solar thermoelectric applications: a first principle study of $CH_3NH_3AI_3$ (A = Pb and Sn). *Chem. Mater.* **26**, 5394–5400 (2014).
33. Wang, Y., Zhang, Y., Zhang, P. & Zhang, W. High intrinsic carrier mobility and photon absorption in the perovskite $CH_3NH_3PbI_3$. *Phys. Chem. Chem. Phys.* **17**, 11516–11520 (2015).
34. Zhang, M., Zhang, X., Huang, L., Lin, H. & Lu, G. Charge transport in hybrid halide perovskites. *Phys. Rev. B* **96**, 195203 (2017).
35. Frost, J. M. Calculating polaron mobility in halide perovskites. *Phys. Rev. B* **96**, 195202 (2017).
36. Kawabata, A. Theory of negative magnetoresistance in three-dimensional systems. *Solid State Commun.* **34**, 431–432 (1980).
37. Lee, P. A. & Ramakrishnan, T. Disordered electronic systems. *Rev. Mod. Phys.* **57**, 287 (1985).
38. Kepenekian, M. & Even, J. Rashba and Dresselhaus couplings in halide perovskites: accomplishments and opportunities for spintronics and spin-orbitronics. *J. Phys. Chem. Lett.* **8**, 3362–3370 (2017).
39. Niesner, D. et al. Giant Rashba splitting in $CH_3NH_3PbBr_3$ organic-inorganic perovskite. *Phys. Rev. Lett.* **117**, 126401 (2016).

Methods

Measurement accuracy analysis. In a standard four-terminal measurement, current is sent through source–drain contacts, and the voltage drop across the sample is measured using two voltage probes. However, if these two voltage probes have a large contact resistance and are not identical, the measurement accuracy could be compromised, especially when the sample resistance is small compared with the contact resistance. Below, we will discuss this argument in detail.

By analysing a four-terminal measurement schematic (Supplementary Fig. 1), the accuracy of the measurement, defined as $\frac{V_{measure}}{V_{real}}$, can be expressed in the following format:

$$V_{real} = V_2 - V_1 \tag{2}$$

$$V_{measure} = V_4 - V_3 = \left(\frac{V_2}{R_c + \delta R_c + R_{im}} - \frac{V_1}{R_c + R_{im}}\right) \times R_{im} \tag{3}$$

so that

$$\frac{V_{measure}}{V_{real}} = \frac{(R_c + R_{im})R_{im} - R_c^2 R_{im} R_{xx} \frac{\delta R_c}{R_c}}{(R_c + R_{im})\left(R_c + R_c \frac{\delta R_c}{R_c} + R_{im}\right)} \tag{4}$$

R_{im} is the internal impedance of equipment. Typically, 10 GΩ is the internal impedance of equipment such as the Keysight SMU B2902A and Keithy 2401. For a lock-in amplifier, for example Stanford Research Systems SR830 and Princeton Applied Research 5210, the internal impedance is 10 MΩ, and can be extended to 10 GΩ if connected in series with a voltage preamplifier.

In this way, the accuracy of the measurement using $R_{im} = 10$ GΩ can be calculated at various contact resistance (R_c) and contact resistance variation ($\delta R_c/R_c$) values for different sample resistances, $R_{xx} = 1.34$ kΩ and 25.7 kΩ, with the results plotted in a colour scale in Supplementary Fig. 1b,c, respectively. In these plots, the green highlights the measurement window with small errors; red and blue show regimes with increasing positive and negative errors, respectively; and the white area highlights the invalid measurement regime. Here 1.34 kΩ is the room temperature sample resistance under 18.8 mW cm^{-2} illumination intensity, and 25.7 kΩ is the resistance under the same illumination condition but measured at 3.5 K. These plots suggest that in order to accurately measure a smaller resistance, a smaller contact resistance or contact resistance variation is required, as manifested as a smaller green area in Supplementary Fig. 1b than in Supplementary Fig. 1c. The black solid lines and the red dashed lines correspond to typical R_c values of a vdW-contact and deposited contact, respectively. These analyses highlight that, with their much lower contact resistance, the vdW-contact devices have a sufficiently large window (the green area) for accurate measurement of the intrinsic transport properties of perovskite materials. For example, when $R_{xx} = 25.7$ kΩ, R_c is 96 kΩ and $\delta R_c/R_c$ is 0.83 (in the sample with the vdW-contact, $\delta R_c/R_c$ changes from 0.16 at room temperature to 0.83 at 3.5 K), corresponding to $\frac{V_{measure}}{V_{real}} = 1.0$ (Supplementary Fig. 1c). On the other hand, there is only a little window to achieve an accurate measurement with the deposited contact due to the excessive contact resistance. For example, if the contact resistance is 232 MΩ, a valid voltage measurement is possible only if $\delta R_c/R_c$ is close to zero (Supplementary Fig. 1c), which is not readily achievable in practice. A slight variation of the contact resistance with $\delta R_c/R_c = 0.1$ leads to a considerable measurement error, with $\frac{V_{measure}}{V_{real}} = -19$.

Materials growth. Vapour phase epitaxial growth has been used to grow single-crystal domains of hybrid perovskite $MAPbCl_3$ (ref. [40]), and subsequently, all-inorganic counterparts[41] and one-dimensional perovskite nanostructures[42], as well as epitaxial thin films on various substrates[43,44]. In the particular case of this work, the precursors, CsBr and $PbBr_2$, were mixed well together with a molar ratio of 1:1. The mixture was brought to 380 °C and the temperature was maintained for 12 h to ensure that the solid-state reaction of the two precursors was completed to form $CsPbBr_3$ powder, which was used for the growth of a $CsPbBr_3$ thin film in a home-built tube furnace system (Thermo Scientific Lindberg Blue M) via a vapour phase deposition process under controlled pressure. The $CsPbBr_3$ powder source was placed at the centre of the furnace in a one-inch quartz tube, and the exfoliated muscovite with its freshly exposed surface was placed downstream as the growth substrate. The system was pumped down and flushed with argon gas three times before being stabilized at 200 mbar with 100 sccm of argon gas as the carrier gas. The furnace was ramped to 560 °C and kept at this temperature for 60 min for the completion of a $CsPbBr_3$ thin film with a thickness of 1 μm (substrate temperature <560 °C).

Materials characterization. Characterizations were carried out using optical microscopy (Olympus BX51), scanning electron microscopy (Zeiss Supra 40 VP, FE-SEM), transmission electron microscopy (Titan S/TEM, FEI; acceleration voltage, 300 kV), X-ray diffraction (Panalytical X'Pert Pro X-ray Powder Diffractometer, Bruker D1 High Resolution Diffractometer with Graded Mirror and Dual (220) Si Incident Beam Optics, Bruker D1 Parallel Beam Diffractometer with Graded Mirror Incidence Beam Optics), AFM (Bruker Dimension FastScan Scanning Probe Microscope) and photoluminescence spectroscopy (Horiba, 488 nm laser wavelength).

Device fabrication. Au electrodes of different geometries with 50 nm thickness were first prepared on a silicon substrate with an atomically flat surface using standard photolithography and high vacuum *e*-beam evaporation. Next, a hexamethyldisilazane (HMDS) layer was applied to functionalize the whole wafer, and then a poly methyl methacrylate (PMMA) layer was spin-coated on top of the Au electrodes. With the pre-functionalization of HMDS, the PMMA layer has weak adhesion to the sacrificial substrate and can be mechanically picked up using thermal release tape, together with the metal electrodes embedded underneath. For a large-area transfer of the entire electrode array embedded in the PMMA layer, the thermal release tape with electrodes was laminated directly to the film and heated to 90 °C to release the PMMA layer. Electron beam lithography (EBL) was applied to make windows on the PMMA layer, exposing the embedded electrode pads for the following electrical measurement. The Au released using this method is atomically flat (replicating the atomically flat surface of the sacrificial wafer), which ensures intimate contact with the atomically flat $CsPbBr_3$ thin film. For the deposit approach, the control device was prepared in an electron beam evaporator. For the mesa isolation, the Hall bar electrodes were prepared with the transfer approach and deposit approach mentioned above. The isolation gaps of the mesa and gaps between each electrode were patterned with EBL and developed in 3:1 isopropanol/MIBK developer. The exposed $CsPbBr_3$ was washed away with 1:1 isopropanol/H_2O solution.

Device characterizations. The device characterization was carried out in a commercial physical property measurement system by Quantum Design. The illumination source was a blue LED installed on the chip carrier, next to the Hall bar, so the relative position between the LED and the Hall bar device was fixed no matter how we flipped the chip carrier in the magnetic field. We also added a black box to cover the device and LED on the rotation stage to prevent any change in reflection from the system chamber. The power density of illumination was determined with a power meter (Newport Optical Power Meter 1916-R with measurement head 818-SL). The electrical measurement was conducted with a precision source/measure unit (Agilent, B2902A) for d.c. measurement and with an SR830 lock-in preamplifier connected with a DL1201 voltage preamplifier for low-frequency a.c. measurement. The four-terminal measurement was performed with an excitation current from 10 nA to 50 nA.

The transient photocurrent measurement was carried out by applying a constant voltage (Yokogawa, GS200) to the device, and a pulsed voltage with a 10 μs width and 50 ms period (Agilent, 33220A) to the LED. The photocurrent was then amplified through the DL1201 current preamplifier and recorded using an oscilloscope (Agilent, DSO3202A). The equivalent circuit diagram is shown in Supplementary Fig. 5a.

Decoupling electron and hole mobility. We assume both types of photogenerated carriers are free carriers with the same density ($n_h = n_e$) since the population of photogenerated carriers are much greater than that of the dark carriers. Based on this assumption, our two-carrier Hall measurement and analysis reveal that the hole mobility is much greater than the electron mobility (~80 times); that is, the hole mobility dictates the overall Hall mobility. The rather low electron mobility suggests that most electrons do not contribute to the charge transport. The method is shown in detail (see Supplementary Fig. 3e,f). The longitudinal and transverse magnetoresistance can be written as follows[13]:

$$\rho_{xx} = \rho_0\left(1 + \mu_h \mu_e B^2\right) = \rho_0 + aB^2 \tag{5}$$

$$\rho_{xy} = B\rho_0(\mu_h - \mu_e) \tag{6}$$

And hereby,

$$\mu_h = \frac{R_H + \sqrt{R_H^2 + 2a\rho_0}}{2\rho_0}, \mu_e = \frac{a}{2\rho_0\mu_h} \tag{7}$$

where μ_h and μ_e are the hole and electron mobility, respectively, B is the magnetic field, R_H is the Hall slope and ρ_0 is the sample resistance at zero magnetic field. Parameter a can be obtained by a quadratic fitting of R_{xx} versus the B curve, and R_H can be calculated using a Hall trace. This offers a way to decouple the hole and electron mobility from the Hall mobility. Following this method and using data shown in Supplementary Fig. 3e,f, we obtained μ_h equal to 395.5 cm^2 V^{-1} s^{-1}, much greater than μ_e, which is 4.537 cm^2 V^{-1} s^{-1}. Here μ_e is only 1.5% of μ_h.

We also note that the electron/hole mobility difference has been recognized in other experiments. For example, the terahertz measurements with extra-porous TiO_2 or AlO_x layers as filters to enable selective measurements in $MAPbI_3$ reveal a hole/electron mobility ratio around six (ref. [25]). Other contactless methods such as the photo illumination quench method reported that the hole/electron mobility ratio is <15 in $FAPbI_3$ (ref. [45]). Overall, these studies show the trend that hole mobility is generally higher than electron mobility, but the actual ratio and exact value are quite different from each other, which further highlights the complexity

of the matter and the critical need to conduct more reliable measurements to fully understand the transport dynamics in halide perovskites.

Evaluation of carrier lifetime and photocurrent gain. We extracted the carrier recombination lifetime τ_{lifetime} through the carrier recombination coefficient following the equation below:

$$\tau_{\text{lifetime}}^{-1} = \gamma_{\text{mono}} + \gamma_{\text{bi}} n \tag{8}$$

We extracted it also from the transient photocurrent following the equation below:

$$I(t) = I_0 \exp(-t/\tau_{\text{lifetime}}) \tag{9}$$

where I_0 is the maximum two-terminal current after pulsed LED illumination.

The photocurrent gain G is defined by the ratio between the generated photocurrent (I_p) and the incident photon flux times elementary charge (I_{ph})[13], leading to the following:

$$G = \frac{I_p}{I_{ph}} = \frac{I_p}{e\left(\frac{PA}{h\nu}\right)} \tag{10}$$

where A is the channel area, P is the illumination power density, h is the Planck constant, e is the elementary charge and ν is the frequency of incident light.

The photocurrent flowing between the electrodes can be expressed as follows:

$$I_p = ne\mu \frac{V}{L} WD \tag{11}$$

where n is the photocarrier density, μ is the carrier mobility, V is the applied voltage and L, W and D are the length, width and thickness of the photoconductor, respectively, with $A = L \times W$.

Assuming one incident phonon generates one electron–hole pair at the steady state, the photogenerated carrier density n relates to its lifetime τ_{lifetime} and incident phonons as follows:

$$n = \tau_{\text{lifetime}} \times \frac{PA}{h\nu} \times \frac{1}{LWD} \tag{12}$$

Plugging equations (11) and (12) into equation (10) results in the following:

$$G = \frac{\mu \tau_{\text{lifetime}} V}{L^2} \tag{13}$$

$$\text{And} \quad \frac{\mu V}{L^2} = \frac{\mu V/L}{L} = \frac{1}{\tau_{\text{transit}}} \tag{14}$$

where the τ_{transit} is the time required for the carrier to travel across the channel of the photoconductor. Therefore, the photocurrent gain is the ratio of carrier lifetime τ_{lifetime} to transit time τ_{transit}, as in the following equation:

$$G = \frac{\mu \tau_{\text{lifetime}} V}{L^2} = \frac{\tau_{\text{lifetime}}}{\tau_{\text{transit}}} \tag{15}$$

Derivation of phase coherence length. We obtained the phase coherence length l_φ using the following equations[37]:

$$\Delta\text{MR}\% = -\alpha\rho \frac{e^2}{2\pi^2\hbar} \sqrt{\frac{eB}{\hbar} F(x)} + \beta B^2 \tag{16}$$

where e is the electronic charge, ρ_0 is the zero-field resistivity, $\hbar$ is the reduced Planck constant, α is a fitting parameter due to Coulomb screening, the last term βB^2 is a correction of the magnetoresistance due to the bulk contribution and $F(x)$ is the Hurwitz zeta function, which can be expressed as follows:

$$F(x) = \sum_{n=0}^{\infty} 2\left(n + 1 + \frac{1}{x}\right)^{\frac{1}{2}} - 2\left(n + \frac{1}{x}\right)^{\frac{1}{2}} - \left(n + \frac{1}{2} + \frac{1}{x}\right)^{-\frac{1}{2}} \tag{17}$$

and

$$x = \frac{4el_\varphi^2}{\hbar} \tag{18}$$

Here we obtain β at 20 K where the weak localization contribution to the MR is suppressed, and fix the value of β through all the temperature range. By tuning the value of x and α, we can obtain the best fitting of ΔMR%. The l_φ at each temperature can then be derived from the corresponding x.

Data availability

The data that support the findings of this study are available from the corresponding author on reasonable request.

References

40. Wang, Y., Shi, Y., Xin, G., Lian, J. & Shi, J. Two-dimensional van der Waals epitaxy kinetics in a three-dimensional perovskite halide. *Cryst. Growth Des.* **15**, 4741–4749 (2015).
41. Zhang, Q. et al. High-quality whispering-gallery-mode lasing from cesium lead halide perovskite nanoplatelets. *Adv. Funct. Mater.* **26**, 6238–6245 (2016).
42. Chen, J. et al. Vapor-phase epitaxial growth of aligned nanowire networks of cesium lead halide perovskites ($CsPbX_3$, X = Cl, Br, I). *Nano Lett.* **17**, 460–466 (2017).
43. Chen, J. et al. Single-crystal thin films of cesium lead bromide perovskite epitaxially grown on metal oxide perovskite ($SrTiO_3$). *J. Am. Chem. Soc.* **139**, 13525–13532 (2017).
44. Jiang, J. et al. Carrier lifetime enhancement in halide perovskite via remote epitaxy. *Nat. Commun.* **10**, 4145 (2019).
45. Eperon, G. E. et al. Formamidinium lead trihalide: a broadly tunable perovskite for efficient planar heterojunction solar cells. *Energy Environ. Sci.* **7**, 982–988 (2014).

Acknowledgements

We thank T. Atallah and J. Caram for discussions. X.D. acknowledges support by the Office of Naval Research through grant no. N00014-18-1-2707 for device fabrications and characterizations, and the US Department of Energy, Office of Basic Energy Sciences, Division of Materials Science and Engineering through award DE-SC0018828 for materials growth. Y.H. acknowledges support by the National Science Foundation EFRI-1433541 for partial support of material preparation. Y. Z. acknowledges support by National Key Research and Development Program of China through grant no. 2018YFA0703503 and National Natural Science Foundation of China through grant no. 51991342 for materials characterizations. I.S. acknowledges the support by the International Scientific Partnership Program at King Saud University (ISPP-148). We acknowledge the Electron Imaging Center at UCLA for transmission electron microscopy technical support and the Nanoelectronics Research Facility at UCLA for device fabrication technical support.

Author contributions

X.D. conceived the research. X.D., Y.W., Q.Q., Z.W. and Y.L. designed the experiments. Y.W., Q.Q. and Z.W. performed the experiments and data analysis. Y.L. and J.G. contributed to device fabrications and initial electrical measurements. Z.K. and I.S. contributed to optical measurement and mobility discussions. Y.K.W. and C.L. conducted the X-ray diffraction measurements. Z.F. and Z.L. contributed to transmission electron microscopy characterizations. C.J. and P.W. helped to make the electrodes. M.G., X.D.D., Y.Z. and Y.H. contributed to discussions and supervised the research. X.D., Y.W. and Q.Q. co-wrote the manuscript. All authors discussed the results and commented on the manuscript.

Competing interests

The authors declare no competing interests.

Additional information

Supplementary information is available for this paper at https://doi.org/10.1038/s41565-020-0729-y.

Correspondence and requests for materials should be addressed to X.D.

Reprints and permissions information is available at www.nature.com/reprints.